



Synthesis and support composition effects on CH₄ partial oxidation over Ni–CeLa oxides



G. Pantaleo^a, V. La Parola^a, F. Deganello^a, P. Calatozzo^b, Rajaram Bal^c, A.M. Venezia^{a,*}

^a ISMN-CNR, Via Ugo La Malfa 153, 90146 Palermo, Italy

^b University of Palermo, Italy

^c Indian Institute of Petroleum, Dehradun, Uttarakhand, India

ARTICLE INFO

Article history:

Received 24 June 2014

Received in revised form 18 August 2014

Accepted 7 September 2014

Available online 16 September 2014

Keywords:

Methane catalytic partial oxidation (CPO)

Ni catalysts

La₂O₃

CeO₂

CeLaO_x

ABSTRACT

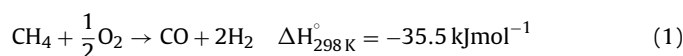
Two series of Ni (6 wt%) catalysts supported over CeO₂, La₂O₃ and mixed CeO₂–La₂O₃ were prepared by co-precipitation and by wet-impregnation. The effect of the two Ni loading procedures on the catalyst structural properties was investigated by XRD, TPR and XPS. The catalytic behavior of the catalysts was tested in the methane partial oxidation reaction performed at 1 atm in a temperature range of 400–800 °C using dilute feed gas mixture with CH₄/O₂ = 2 and gas hourly space velocity of 60,000 ml g^{−1} h^{−1}. Total methane combustion was observed within the 450 °C ≤ T ≤ 650 °C temperature range. Above 650 °C partial oxidation of methane started to occur, reaching at 800 °C a CO selectivity close to 90%. The lanthanum containing catalysts prepared by wet impregnation exhibited higher CPO activity at lower temperature as compared to the co-precipitated ones. Opposite behavior was observed with the Ni–CeO₂ catalysts. During the stability test at high temperature, carbon formed only over the single oxide supported catalysts, Ni–CeO₂ and Ni–La₂O₃. According to the characterization results carbon was not responsible for catalyst deactivation but it prevented the sintering of the nickel particle. The interplay of the crystallite sizes and the formation of various nickel–lanthanum oxide species with different Ni oxidation states were responsible for the differences in the CPO performance.

© 2014 Elsevier B.V. All rights reserved.

1. Introduction

The production of synthesis gas from natural gas is an important step in the gas to liquid (GTL) technology, accounting for 50–75% of the capital cost. The syngas may be actually produced by different processes such as steam reforming (SR), dry reforming (DR), partial oxidation of methane (POM) and autothermal reforming (ATR) which is a combination of the endothermic reforming reaction (SR) and the exothermic oxidation reaction [1–3]. Dry reforming is an interesting and promising process since it contributes to the removal of the greenhouse CO₂ present in the natural gas in a 2% amount [4]. However the difficulty to activate the stable CO₂ molecule and to avoid catalyst poisoning by the large amount of carbon deposition still prevents its application at industrial level. In fact, each of the mentioned processes presents peculiarity in terms of the produced H₂/CO ratio, carbon poisoning and energy efficiency. However, steam reforming (SR) and catalytic partial oxidation of methane (POM) are currently the preferred reactions

to produce synthesis gas. With respect to the endothermic steam reforming, which is highly energetic and capital intensive [5,6] the partial oxidation reaction (1)



offers the following advantages: (a) H₂/CO ratio of 2, suitable for methanol or Fischer–Tropsch synthesis; (b) being mildly exothermic the CPO process does not require large heat exchange reactors and needs a more compact plant technology [7]. Nevertheless, as for all the reactions involving conversion of methane the choice of a catalyst, able to activate the molecule, is crucial due to the high dissociation energy of the first CH₃–H(g) bond (440 kJ/mol) [8]. Noble metals are appropriate for this kind of reaction, exhibiting high activity/selectivity and long term stability. However, since noble metals are rather expensive their use is prohibitive for industrial application. A more convenient alternative is represented by nickel which is also active but less stable, suffering from carbon deposition and metal sintering [5,9]. Still, in terms of cost and availability, the nickel based catalysts are the most interesting systems and much research is being addressed to their stability improvement [9]. To this respect the choice of an appropriate support is very

* Corresponding author. Tel.: +39 0916809372; fax: +39 0916809399.
E-mail address: venezia@pa.ismn.cnr.it (A.M. Venezia).

important as the supports affect the metal dispersion, inhibit particle sintering and in the case of basic character they may minimize carbon formation [10]. Different types of oxides like Al_2O_3 , MgO , La_2O_3 and CeO_2 have been investigated as nickel supports for CPO applications [11–17]. These oxides differ for oxygen mobility and for their different degree of interaction with nickel, both properties affecting the catalyst reducibility and their final catalytic behavior. According to the literature no definite conclusion on the most suitable support can be drawn. Indeed, the use of a specific support has yielded different catalytic results related to various factors such as the precursor of the catalyst components, the preparation methods, the nickel loading and the CPO reaction conditions.

The objective of the present study was to analyze the effect of the synthesis procedure and the effect of the nature of the support on the catalytic behavior of Ni over CeO_2 , La_2O_3 and mixed oxide CeO_2 – La_2O_3 . The two oxides were selected because of their peculiar properties. CeO_2 is characterized by large oxygen mobility, playing an important role in the oxidation type of reaction [18,19]. La_2O_3 is characterized by a strong chemical interaction with nickel, forming several La–Ni oxide phases and therefore stabilizing the metal and possibly avoiding carbon formation [20,21]. The catalytic results in terms of methane conversion and CO selectivity were related to the structural and chemical properties of the samples investigated by XRD, XPS and TPR techniques.

2. Experimental

2.1. Sample preparation

2.1.1. Support preparation

La_2O_3 , CeO_2 and $\text{La}_2\text{O}_3/\text{CeO}_2$ (Ce/La = 50/50 wt%) oxides were prepared by (co)-precipitation from the corresponding nitrate precursors using K_2CO_3 to precipitate the corresponding hydroxides. After washing several times to remove the potassium and drying at 100°C , the obtained solids were calcined at 800°C for 4 h.

2.1.2. Catalyst preparation

Two series of catalysts were prepared by following two procedures. One series was prepared by wet impregnation (WI) consisting of impregnating the supports with $\text{Ni}(\text{NO}_3)_2$ aqueous solution, of the appropriate concentration to obtain a final catalyst with 6 wt% Ni. The solid was dried overnight at 100°C and then calcined at 800°C for 4 h. The other series was prepared by co-precipitation (CP) with the procedure used for the supports alone except for adding $\text{Ni}(\text{NO}_3)_2$ to the rare earth nitrate solution. All the reagents were from Aldrich. The obtained samples were labeled as Ni–La and Ni–Ce and Ni–CeLa followed by the notation of (CP) or (WI).

2.2. Sample characterization

The specific surface area of the supports were determined from N_2 adsorption–desorption isotherms at -196°C using a Sorptomatic 1900 (Carlo Erba) instrument through the Brunauer–Emmett–Teller (BET) calculation methods [22]. Before the measurements, samples were heated in vacuum at 250°C for 2 h.

The phase composition of crystalline components of fresh and spent samples was investigated by X-ray diffraction (XRD) analyses and Rietveld refinement. XRD patterns were recorded in Bragg–Brentano para-focusing geometry using a Bruker D5000 diffractometer, equipped with $\text{Cu K}\alpha$ anode and graphite monochromator. The XRD data were collected in the angular range 10 – 80° in 2θ using 0.05° step size and counting time of 5 s per step. The assignment of the various crystalline phases was based on the JPDFS powder diffraction file cards [23]. The diffraction patterns

were analyzed by Rietveld refinement using the GSAS package [24]. Chebyshev polynomials and Pearson VII functions were chosen for the background and for the peak profile fitting, respectively. In the structure refinement, lattice constants, zero offset, scale factors and full width half maximum (FWHM) were considered as variable parameters. From fitting results, the structural parameters of the investigated compounds and, in particular, the cell edge lengths and the relative phase composition were obtained. An estimation of the mean crystal size values was obtained from the line broadening calculated by Rietveld analysis in agreement with the GSAS package procedure [24] and with the Scherrer equation [25].

Temperature programmed reduction (TPR) experiments were carried out with a Micromeritics Autochem 2910 apparatus equipped with a thermal conductivity detector (TCD). The gas mixture with composition 5% H_2 in Ar (30 ml/min) was used to reduce the samples (50 mg), heating from room temperature to 800°C at the rate of $10^\circ\text{C}/\text{min}$. Before starting the TPR analyses, the catalysts were pretreated with a flowing gas mixture of 5% O_2 in He (50 ml/min) at 550°C for 30 min, then cooling down under He.

The thermogravimetric analyses (TGA) were performed in O_2 using the TGA 1 Star System of Mettler Toledo. About 5 mg of sample was heated from room temperature to 1100°C at the rate of $10^\circ\text{C}/\text{min}$. The evolution of the CO_2 was monitored by mass quadrupole.

The X-ray photoelectron spectroscopy (XPS) analyses of the calcined and spent catalysts were performed with a VG Microtech ESCA 3000 Multilab, equipped with a dual Mg/Al anode. The spectra were excited by the unmonochromatised Mg $\text{K}\alpha$ source (1253.6 eV) run at 14 kV and 15 mA. The analyzer operated in the constant analyzer energy (CAE) mode. Survey spectra were measured at 50 eV pass energy. For the individual peak energy regions, a pass energy of 20 eV set across the hemispheres was used. The sample powders were mounted on a double-sided adhesive tape. The pressure in the analysis chamber was in the range of 10^{-8} Torr during data collection. The constant charging of the samples was corrected by referencing all the energies to the C 1s peak energy set at 285.1 eV, arising from adventitious carbon. Analyses of the peaks were performed with the software provided by VG, based on non-linear least squares fitting program using a weighted sum of Lorentzian and Gaussian component curves after background subtraction according to Shirley and Sherwood [26,27]. Atomic concentrations were calculated from peak intensity using the sensitivity factors provided with the software. The binding energy values are quoted with a precision of ± 0.15 eV and the atomic percentage with a precision of $\pm 10\%$.

2.3. Catalytic measurements

Methane oxidation catalytic tests were performed using a U shaped quartz reactor with an inner diameter of 12 mm, electrically heated in a furnace. The catalyst powder (sieved fraction between 180 and $250\ \mu\text{m}$) was diluted 1:2 with inert SiC, in order to avoid thermal gradients. The reaction temperature was measured by a K-type thermocouple in contact with the catalytic bed long 12 mm. Prior to the catalytic testing, the samples were treated “in situ” under flowing O_2 (5 vol.% in Ar, 50 ml/min) at 350°C for 1/2 h. After cooling down to room temperature, the samples were reduced under flowing H_2 (5 vol.% in He, 50 ml/min) increasing the temperature to 750°C with a $10^\circ\text{C}/\text{min}$ ramp and a holding time of 1 h. The feed gas consisting of 2 vol.% of CH_4 + 1 vol.% O_2 in He, was led over the catalyst (50 mg) at a flow rate of 50 ml/min (STP), equivalent to a weight hourly space velocity (WHSV) of $60,000\ \text{ml g}^{-1}\ \text{h}^{-1}$. The activities were measured as a function of temperature from 400°C to 800°C with a heating rate of $10^\circ\text{C}/\text{min}$.

For detection signal stabilization, at the chosen interval of 50°C the temperature was held for 30 min, thereafter the signals were

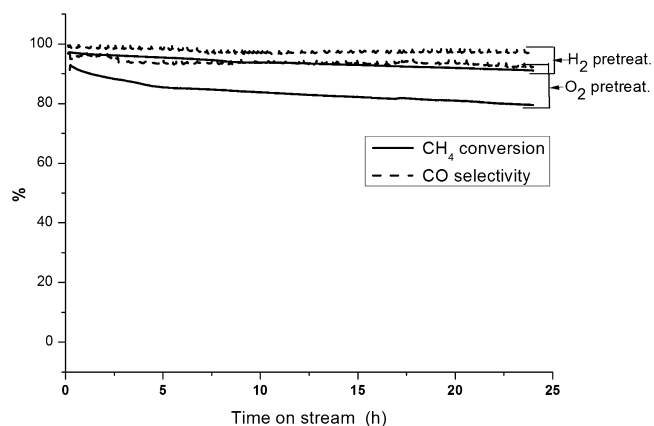


Fig. 1. Effect of oxidation and reduction treatment on catalytic activity of Ni-CeLa(WI) measured at 800 °C.

reported and plotted as function of the temperature. For the long run measurements the samples were brought into contact with the reaction mixture directly at 800 °C and kept at this temperature for 24 h. The inlet and outlet gas compositions were analyzed by on line mass quadrupole (ThermostarTM, Balzers), in order to follow the evolution of all the species, CH₄, CO, CO₂, H₂, H₂O, O₂. Moreover, the concentrations of CO, CO₂ and CH₄ species were checked by IR analysers (ABB Uras 14, Uras 26), calibrated in the range 0–3000 ppm for CO, 0–10,000 ppm for CO₂ and 0–30,000 ppm for CH₄. Carbon balance was close to $\pm 5\%$ in all the catalytic tests. The methane conversion X_{CH_4} and the selectivity to CO S_{CO} were calculated as $X_{CH_4} = (CH_4^{in} - CH_4^{out}) / CH_4^{in} \times 100$ and $S_{CO} = CO / (CO + CO_2) \times 100$ respectively.

3. Results and discussion

3.1. Catalyst activity

Preliminary tests were performed on reduced and on just oxidized samples. The reduced ones were pretreated in H₂/Ar at 750 °C as described above. The oxidized ones were simply treated in 5% O₂ in He at 400 °C for 30 min. As shown in Fig. 1 for the selected sample, Ni-CeLa(WI), the methane conversion and the CO selectivity during a long run at 800 °C were definitively better on the reduced sample as compared to the unreduced one. Based on these results, all the catalytic tests reported here were performed on

reduced samples. The performance of the different catalysts, in terms of methane conversion and products (CO and CO₂) selectivity as function of temperature, are shown in Figs. 2–4. In the range of temperature between 450 °C and 650 °C all the catalysts were active in the total oxidation of methane, reaching the methane conversion of $\sim 25\%$, the maximum allowed by the stoichiometry of the methane combustion reaction ($CH_4/O_2 = 0.5$) with complete oxygen consumption. Beyond this temperature range, catalytic partial oxidation of methane was occurring reaching methane conversion and CO selectivity close to the thermodynamic equilibrium values [5,28]. By comparing the plots in Fig. 2 referring to the Ni supported over La₂O₃ with the plots in Fig. 3 referring to the Ni supported over the mixed oxides CeO₂–La₂O₃, it is obvious that in both cases the method of wet impregnation (WI) yielded catalysts with a light-off temperature for the CPO reaction lower (by 50 °C and 100 °C respectively for the two different supports) than for the catalysts prepared by co-precipitation. In the case of the nickel catalyst supported on CeO₂, the opposite behavior was observed. Indeed as shown in Fig. 4a and b, the sample prepared by CP exhibited a 50 °C lower CPO light off temperature as compared to the corresponding sample prepared by WI. However, the Ni-Ce(CP) deactivated quite quickly with the increasing temperature.

The catalyst stability was checked by monitoring the catalytic reaction at 800 °C for a period of 24 h. A typical time on stream curve (TOS) was given in Fig. 1. The results for the all samples are summarized in Fig. 5 with a bar diagram of the methane conversion attained after 24 h, versus the two preparation procedures for the different catalyst formulations. Except for the Ni-La(CP) sample maintaining the highest methane conversion after 24 h, for the other two formulations the wet impregnated catalysts remained more active with respect to the co-precipitated ones.

3.2. Characterization of catalysts

3.2.1. XRD analyses

The specific surface area of the catalysts determined by the BET method are listed in Table 1 along with the structural properties such as crystalline phases and corresponding sizes and weight percentages obtained from the Rietveld analysis. As expected from samples being calcined at 800 °C, the surface areas were rather low [20]. The structural properties of the different catalysts were investigated by X-ray diffraction analyses performed on the fresh (calcined) and on the aged catalysts after the stability test.

As shown in Fig. 6 for the Ni-La samples, different phases were formed depending on the two preparation procedures. The Rietveld

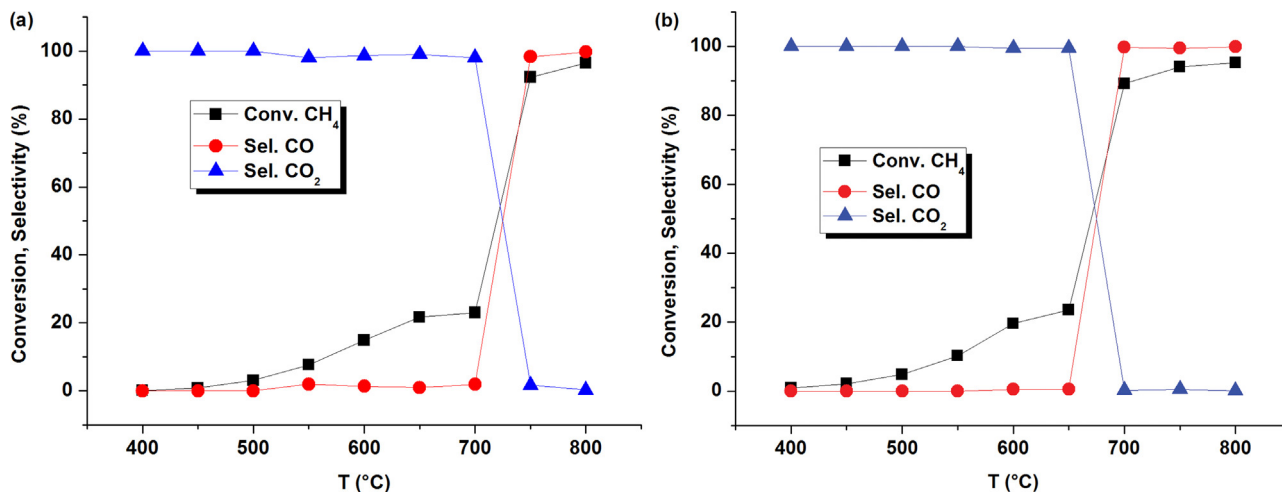


Fig. 2. CH₄ conversion and selectivity to CO and CO₂ as a function of temperature in partial oxidation of methane over: (a) Ni-La₂O₃ (CP); (b) Ni-La₂O₃ (WI).

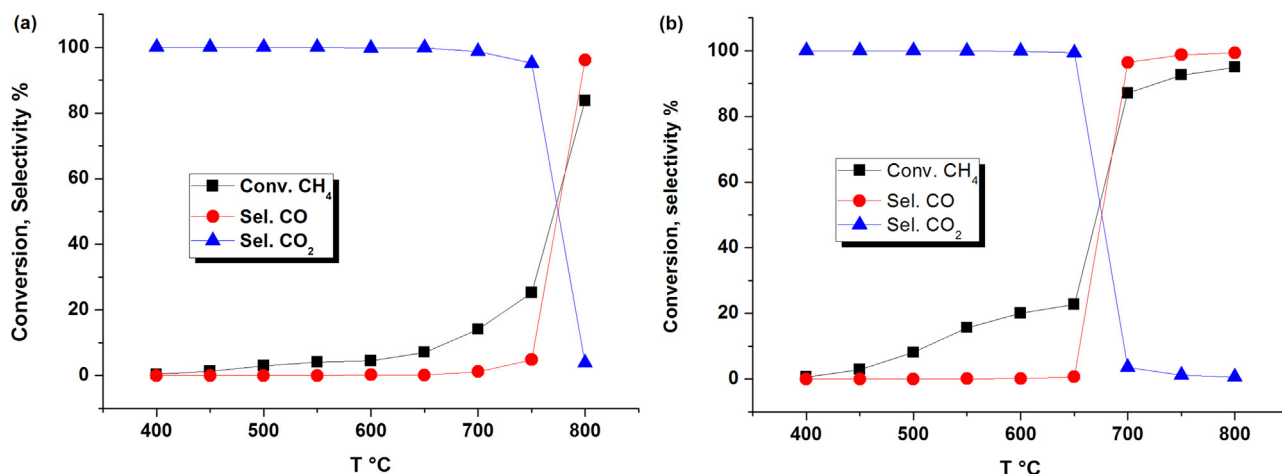


Fig. 3. CH₄ conversion and selectivity to CO and CO₂ as a function of temperature in partial oxidation of methane over: (a) Ni-CeLa (CP); (b) Ni-CeLa (WI).

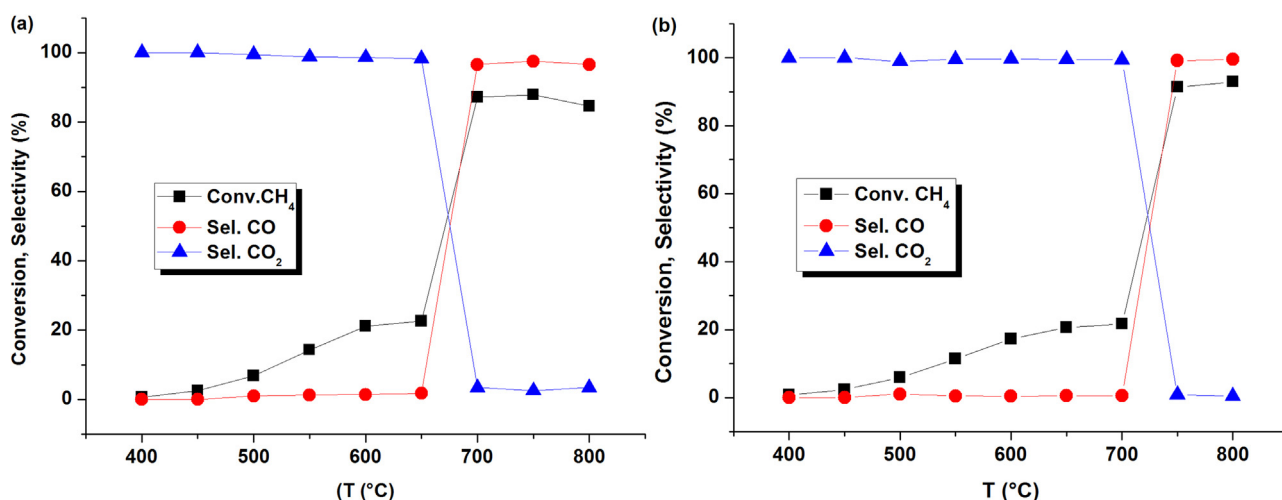


Fig. 4. CH₄ conversion and selectivity to CO and CO₂ as a function of temperature in partial oxidation of methane over: (a) Ni-CeO₂ (CP); (b) Ni-CeO₂ (WI).

refinement analyses allowed to discern clearly in both samples the hexagonal La₂O₃ oxide as main phase characterized by crystallite size of 85 nm and of 56 nm in the CP and the WI sample respectively. Moreover the co-precipitated sample (Fig. 6a) contained NiO (3 wt%) and a variety of mixed La–Ni oxides phases such as LaNiO₃ (7 wt%), La₂NiO₄ (6 wt%), orthorhombic La₄Ni₃O₁₀ (8 wt%), and La₃Ni₂O₇ (4 wt%). In order to look for possible relationship between the catalytic activity and the Ni precursor oxidation state, an average Ni oxidation state was estimated, assuming that all

the nickel was present in the crystalline phase detected by the XRD and not as undetectable amorphous species. Such assumption was corroborated by the Rietveld derived Ni over Ce and/or La atomic ratios, being close to the analytical ones or even slightly higher as in the case of the Ni–CeLa materials. Considering the molar percentage and the formal Ni oxidation state for each phases a weighted average of the Ni oxidation number of +2.5 was calculated for the Ni–La(CP). The impregnated sample (Fig. 6c) was formed by larger amount of La₂NiO₄ (20%), La₄Ni₃O₁₀ (13%), La₃Ni₂O₇ (9.6%) and

Table 1

Specific surface area (BET), Ni containing phases, support phases and corresponding crystallite sizes with phase percentages (%) in parentheses.

Catalysts	BET (m ² /g)	Ni phases crystallite size (nm) ^a				Support crystallite size (nm)				
		Fresh ^b		Aged ^c		Fresh		Aged		
		NiO	La _x Ni _y O _z	NiO	Ni	La ₂ O ₃	CeO ₂	Ce _x La _{1-x} O _a	La ₂ O ₃	CeO ₂
Ni–La(CP)	5	25 (3)	20 (26)		16 (4)	85 (71)				
Ni–La(WI)	4	–	20 (44)		20 (5)	56 (55)			35 (75)	27 (20)
Ni–CeLa(CP)	6	31 (6)	33 (14)		44 (7)			33 (80)	37 (93) ^d	
Ni–CeLa(WI)	4	17 (11)	34 (4)		30 (8)			35 (84)	27 (92) ^d	
Ni–Ce(CP)	6	35 (9)	–	72 (2)	53 (7)	56 (91)			73 (93)	
Ni–Ce(WI)	5	45 (9)	–		34 (7)	122 (91)			104 (93)	

^a The crystallite sizes and the corresponding phase percentage (%) are calculated by the Rietveld refinement analysis.

^b After calcinations at 800 °C.

^c After long term stability test.

^d this size refer to the CeLaO_x phase.

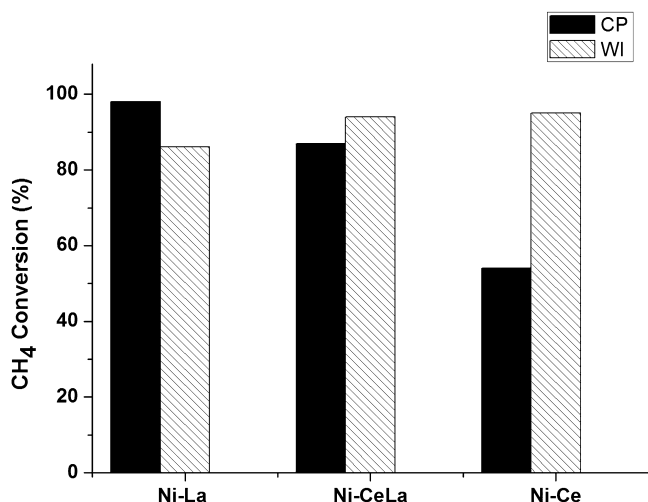


Fig. 5. Methane conversion measured at 800 °C after 24 h on stream as a function of the preparation procedure for the different catalyst formulation.

quite small amount (1.5%) of perovskites with a weighted average oxidation state of nickel around +2.3. As shown in Fig. 6b and d the catalytic reaction induced drastic change of the sample structure. Indeed, according to the given XRD pattern in Fig. 6b, all the La_2O_3 reflections of the aged Ni-La(CP) sample were replaced by those relative to $\text{La}(\text{OH})_3$ phase. Any $\text{La}_x\text{Ni}_y\text{O}_z$ related peaks vanished whereas Ni metal peaks were discernable. The Rietveld refinement of the pattern indicated crystallite sizes of 20 nm for the lanthanum hydroxide, quite smaller with respect to the parent La_2O_3 (85 nm) crystallites, and about 16 nm for the metallic Ni, comparable with the precursor NiO size. According to Fig. 6d the Ni-La(WI) after reaction underwent partial modification of the support structure maintaining both the La_2O_3 and $\text{La}(\text{OH})_3$ phases. According to the Rietveld refinement, the oxide and hydroxide relative compositions were respectively 75 wt% and 20 wt% with crystallite sizes of 35 nm and 27 nm respectively. Hardly visible Ni metal peaks corresponding to crystallites of about 20 nm were present.

The XRD patterns of the calcined Ni-CeLa samples are shown in Fig. 7. Definitely the co-precipitation of Ce^{3+} and La^{3+} hydroxides produced cubic $\text{Ce}_x\text{La}_{1-x}\text{O}_a$ mixed oxide with La^{3+} replacing Ce^{4+} ions of the fluorite lattice of the ceria [29]. Both samples

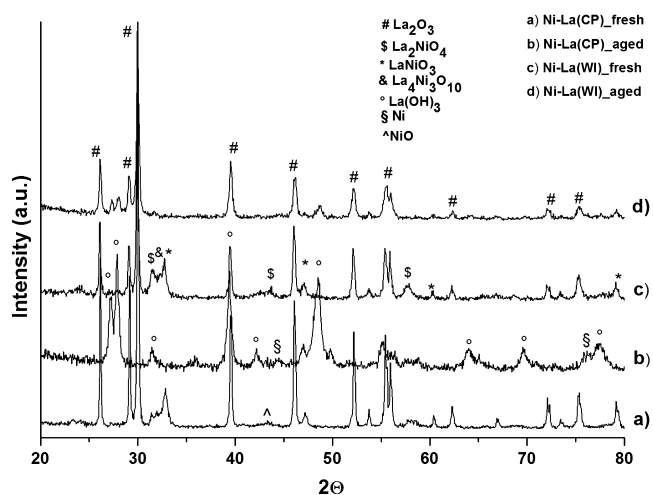


Fig. 6. XRD patterns of the fresh and aged Ni-La samples. The main reference peaks from ICSD patterns (La_2O_3 no. 96196; $\text{La}(\text{OH})_3$ no. 31584; La_2NiO_4 no. 33526; LaNiO_3 no. 67714; $\text{La}_4\text{Ni}_3\text{O}_{10}$ no. 80279; Ni no. 41508; NiO no. 9886) are indicated.

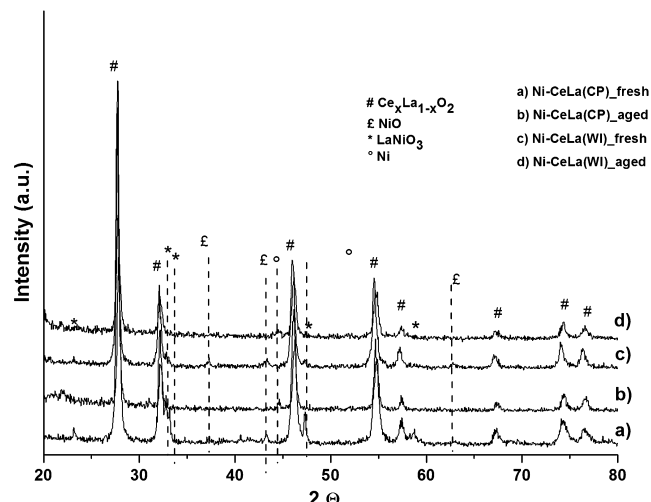


Fig. 7. XRD patterns of the fresh and aged Ni-CeLa samples. The main reference peaks from ICSD patterns ($\text{Ce}_{0.56}\text{La}_{0.44}\text{O}_{1.78}$ no. 77910; NiO no. 9886; LaNiO_3 no. 67714; Ni no. 41508) are indicated.

contained Ce enriched mixed phases with an x value ranging from 0.55 to 0.66 and with a larger lattice parameter as compared to CeO_2 as a consequence of the larger radius of La^{3+} (1.16 Å) with respect to Ce^{4+} (0.97 Å) [30]. Indeed, according to the results from Rietveld refinement, with respect to the 5.412 Å value obtained for the CeO_2 prepared by precipitation, the lattice parameter value of the $\text{Ce}_x\text{La}_{1-x}\text{O}_a$ phase was between 5.542 and 5.582 Å depending on the x value. From the line broadening analyses, as reported in Table 1, the sizes of the $\text{Ce}_x\text{La}_{1-x}\text{O}_a$ crystallites were of the order of 33–35 nm for both samples, smaller than the crystallite sizes obtained for the separate oxide phases in the single oxide supported catalysts. Moreover, perovskite LaNiO_3 and NiO phases were present. The Rietveld analyses of the diffractograms allowed to quantify for the CP sample a larger amount of perovskite (14.2%) and lower amount of NiO (5.6%) as compared to the reverse situation of the wet impregnated one with 4.2% perovskite and 11.5% of NiO. The estimated Ni average oxidation number was +2.4 in the co-precipitated sample and +2.1 in the impregnated sample. With respect to this point, it is interesting to note that the wet impregnated series of the La_2O_3 and the mixed CeO_2 – La_2O_3 supported catalysts, being more active in the CPO reaction, were characterized by a smaller Ni average oxidation state. Upon catalytic reaction, as observed from the patterns of the aged samples, both catalysts underwent reduction of the Ni^{3+} and Ni^{2+} containing phases into metallic Ni with complete removal of the perovskite phase. De-mixing of the composite $\text{Ce}_x\text{La}_{1-x}\text{O}_a$ oxide did not occur.

The XRD patterns of the calcined Ni-Ce samples are shown in Fig. 8. Reflections related to the fluorite structure of the CeO_2 and peaks belonging to the NiO phase were present. The Rietveld refinement of the XRD curves yielded for the two differently prepared samples the same lattice parameters of the pure CeO_2 . The absence of cell contraction which would be caused by the incorporation of the Ni^{2+} (ionic radius of 0.072 nm) into the cubic structure of CeO_2 (Ce^{4+} ionic radius of 0.101 nm) excluded solid solution formation [12,31]. As shown in Table 1, the main obvious difference was the size of the CeO_2 crystallites which in the Ni co-precipitated catalyst was much smaller (56 nm) as compared to the impregnated catalyst (122 nm). It followed from this observation, in accord with the literature [31], that the incorporation of Ni^{2+} by co-precipitation inhibited the crystal growth of the fluorite structure during the calcination treatment. A mutual influence of nickel and ceria was also evident in the pattern of the aged co-precipitated sample

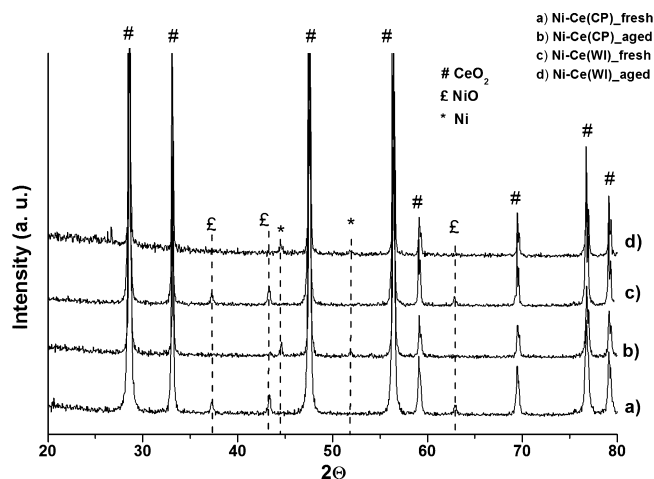


Fig. 8. XRD patterns of the fresh and aged Ni–Ce samples. The main reference peaks from ICSD patterns (NiO no. 9886; CeO₂ no.180851; Ni no. 41508) are indicated.

Ni–Ce(CP). In this case, differently from the impregnated sample, besides peaks due to metallic nickel also some small but still identifiable peaks due to NiO were observed. As given in Table 1, the smaller CeO₂ crystallites present in the fresh Ni–Ce(CP) sample, in

Table 2

*T*_{max} and H₂ consumption volumes (*V*) of the TPR peaks obtained for the different Ni samples.

Catalyst	<i>T</i> _{max} (°C)		<i>V</i> (ml/g _{catal})	
	1st peak	2nd peak	1st peak	2nd peak
Ni–La(CP)	345	535	13	18
Ni–La(WI)	355	578	5	19
Ni–Ce(CP)	350	509	19	6
Ni–Ce(WI)	372	478	20	7
Ni–CeLa(CP)	346	453	18	12
Ni–CeLa(WI)	381	469	18	7

closer contact with the nickel oxide were probably inhibiting the complete reduction of the nickel.

3.2.2. TPR analyses

Temperature programmed reduction measurements were carried out in order to determine the reducibility of the Ni species deposited by the two different techniques in the supports. The H₂-TPR profiles are displayed in Fig. 9. The reduction peak temperatures and the corresponding H₂ consumption volumes are summarized in Table 2. The profiles of the Ni–Ce(CP) and the Ni–Ce(WI), shown in Fig. 9a, are characterized by two peaks, one at low temperature due to the reduction of large NiO particles and the other at higher temperature due to smaller NiO in intimate contact

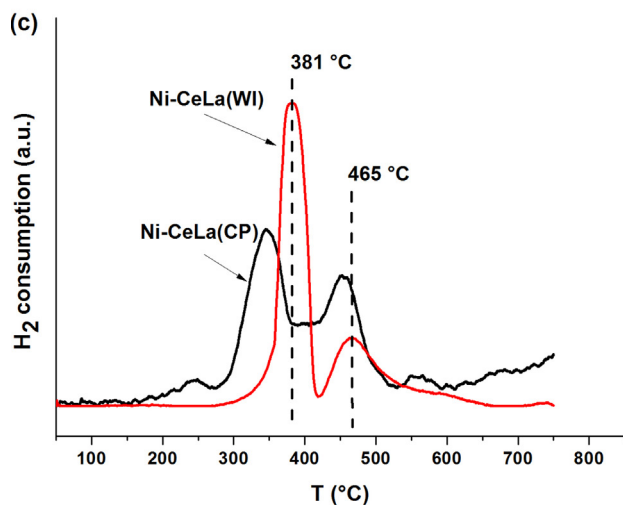
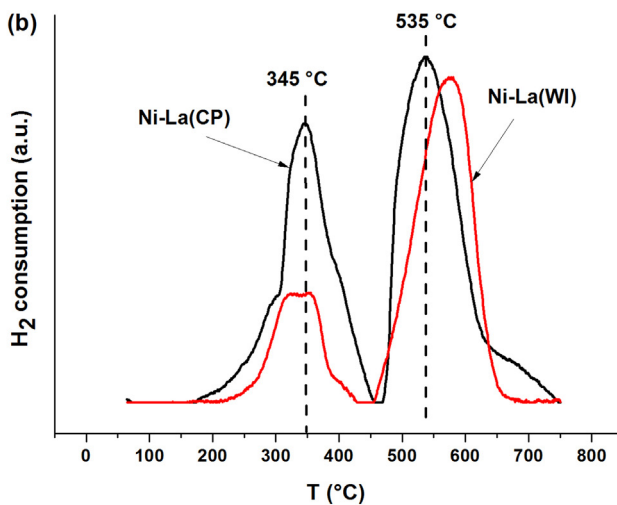
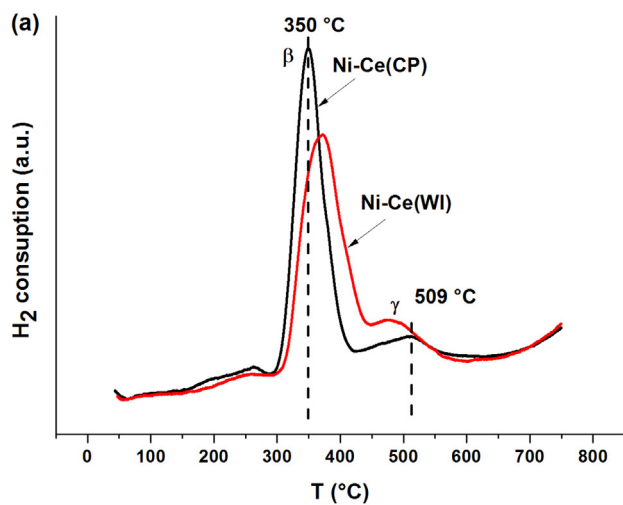


Fig. 9. TPR profiles of the differently prepared samples calcined at 800 °C (a) Ni/CeO₂; (b) Ni/La₂O₃; (c) Ni/CeLaO_x.

with the oxide support [32]. A contribution to the high temperature peak might also arise from the ceria surface reduction [16]. The slight differences between the two sample TPR curves were attributed to morphology effect considering that in the CP sample the nickel was more uniformly distributed among the smaller CeO₂ crystallites, giving rise to a narrower TPR peak as compared to the WI sample. As seen in Table 2, the H₂ consumption for the two catalysts were quite similar and close to the expected value of 24 ml/g_{cat} calculated on the bases of the analytical Ni concentration. The rising curve at high temperature was attributed to the reduction of the ceria support occurring above 700 °C [29]. The TPR data of the Ni–Ce samples were therefore in perfect accord with the XRD analyses excluding formation of Ce_{1-x}Ni_xO₂ solid solution. Indeed, in such case a strong modification of the TPR pattern with respect to the NiO pure phase should have been observed [31].

The TPR profiles of the Ni–La₂O₃ samples calcined at 800 °C are shown in Fig. 9b. As for the Ni–CeO₂ samples, these profiles suggested two consecutive steps reduction [33]. Obviously there was a strong effect of the preparation procedure on the reducibility curves. Considering the large variety of the Nickel containing phases, detected by the XRD as discussed previously, the attribution of the peak to a particular nickel species was quite difficult. In the case of a single perovskite phase the low temperature peak at 320–355 °C would have been assigned to the first reduction of the Ni³⁺ within the perovskite structure to Ni²⁺ of the spinel structure La₂NiO₄ [21]. The high temperature peak at 535–570 °C would have been attributed to the reduction of Ni²⁺ to metallic nickel. However according to a different interpretation, the low temperature peak of the TPR pattern of a Ni–La₂O₃ system calcined in O₂ at 800 °C could be due to the reduction of amorphous NiO whereas the high energy peak to the reduction of the perovskite LaNiO₃ [14]. In the present systems, the peaks would reflect the average situation of the multiple oxidation state of the nickel. Both the co-precipitated sample Ni–La(CP) and the impregnated sample Ni–La(WI) exhibited similar reduction profile except for the quite smaller peak in the range of 320–355 °C of the impregnated samples. The larger total H₂ consumption of the Ni–La(CP) sample as compared to the Ni–La(WI) sample, as shown in Table 2, reflected a different distribution of the various nickel species, and according to the XRD analyses, the larger Ni average oxidation state of the fresh Ni–La(CP).

The TPR profiles of the mixed oxide supported nickel catalysts are given in Fig. 9c. The reduction curve of the Ni–CeLa(WI) sample was similar to those obtained for the nickel over pure ceria, with a stronger peak at 381 °C and a smaller peak at 469 °C. The curve of the Ni–CeLa(CP) sample was more complex with two main peaks of similar intensity, one at 346 °C and the other one at 453 °C as given in Table 2. The wide gap between the two peaks suggested the presence of an intermediate temperature reduction peak. By the same arguments used for the Ni–La samples, the larger total H₂ consumption of the Ni–CeLa(CP), given in Table 2, reflected the larger Ni average oxidation state of the CP sample with respect to the WI sample, as estimated from the XRD analyses. Moreover, differences in the reduction peak temperatures (*T*_{max}) were related to differences in the size of NiO particles.

3.2.3. TGA analyses

The thermogravimetry curves of Ni–Ce, Ni–La and Ni–CeLaO_x prepared by the two different methods after the stability test performed at 800 °C are given in Fig. 10. The TGA curves, of the two Ni–La samples, coupled with the CO₂ mass quadrupole detection, clearly denoted a weight loss due to the removal of carbon. For both samples, three distinct steps at 350 °C, at 487 °C and at 664 °C corresponding to three different types of carbon species formed on the samples, were observed in agreement with literature results [34]. At variance with the cited literature none of the carbon species could be attributed to crystalline La₂O₂CO₃, since no evidence of

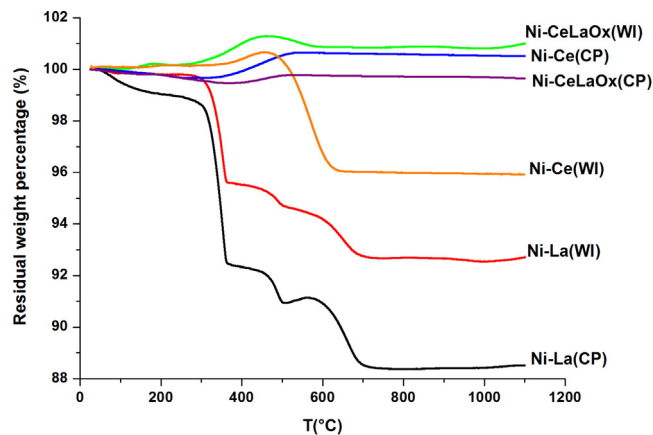


Fig. 10. TGA profiles of differently prepared Ni/CeO₂, Ni/La₂O₃, Ni/CeLaO_x.

this phase was found in the XRD of the aged samples. Nevertheless the presence of such species in amorphous state could not be discarded. With the exception of the Ni–Ce sample prepared by impregnation, exhibiting a weight loss of 4.7% in the temperature range between 450 °C and 500 °C, the TGA curves of the Ni–Ce(CP) and of both Ni–CeLa samples were quite different. The curves did not present any weight loss but only a slight weight gain, in the temperature range 400–450 °C, likely due to the oxidation of Ce³⁺ previously formed in the reducing atmosphere of the catalytic test. Based on these TGA data, the catalyst deactivation observed in particular with the Ni–Ce(CP) catalyst could not be related to carbon formation. The close examination of the weight loss reported in Fig. 10 and the Ni crystallite sizes of the aged samples listed in Table 1 suggested that the carbon deposition prevented nickel sintering, to which the rapid deactivation of the Ni–Ce(CP), after the stability test at 800 °C, could be ascribed.

3.2.4. XPS analyses

The XPS results are summarized in Table 3, where the main binding energies and the atomic ratio Ni/(Ce + La) are listed. In the last two columns of the atomic ratios the corresponding values after reactions are given in parentheses. The experimental Ni 2p_{3/2} X-ray photoelectron spectra with the fitted curves of the Ni–Ce samples as fresh (calcined at 800 °C) and after reaction are displayed in Fig. 11. The energy region contained the Ni 2p_{3/2} component and the broad energy shake up satellite peak ~6 eV above the main line, typical

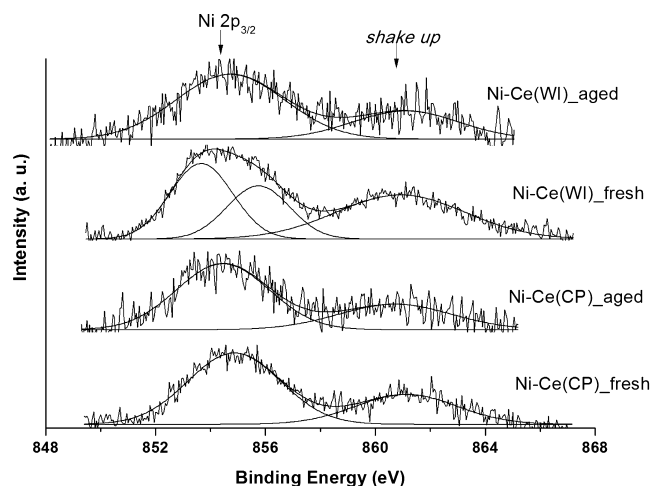


Fig. 11. Ni 2p XP spectra of Ni–Ce(CP) and Ni–Ce(WI) before and after the catalytic reaction.

Table 3
Main XP peak binding energies and derived atomic ratio of the various Ni catalysts.

Samples	La 3d _{5/2}	Ni 2p _{3/2}	Ni 3p	O 1s	Ce 3d _{5/2}	La/Ce ^a	Ni/(Ce + La) ^{a,b}
Ni–La(CP)	834.4	–	67.9	531.6 528.9	–	–	0.15 (0.16)
Ni–La(WI)	834.5	–	68.2	531.5 528.7	–	–	0.14 (0.17)
Ni–Ce(CP)	–	854.5	67.7	529.5 531.7	882.3	–	0.39 (0.16)
Ni–Ce(WI)	–	853.6 855.7	67.4	529.5 531.9	882.2	–	1.23 (0.35)
Ni–CeLa(CP)	834.0	–	68.3	528.9 531.6	881.4	1.1 (1.7)	0.22 (0.11)
Ni–CeLa(WI)	834.5	–	67.9	528.6 531.4	881.2	0.7 (2.6)	0.57 (0.27)

^a The values in parentheses refer to the ratio after the stability test at 800 °C.

^b Obtained from Ni 3p XP peak.

of oxidized nickel. The spectrum of the co-precipitated sample was characterized by the Ni 2p_{3/2} peak at 854.4 eV. The better quality of the spectrum of the impregnated sample Ni–Ce(WI), allowed to fit the experimental curve with two components one at 853.6 eV still attributable to NiO and a weaker component at 855.7 eV typical of Ni(OH)₂ [35]. After catalytic reaction the binding energy of the Ni 2p peak did not change, whereas its intensity decreased substantially for both samples. The apparent contradiction with the XRD detection of metallic nickel after reaction was justified by the different information depth of the two techniques with XPS probing the very top layers, easily re-oxidized even after a short exposure to air, and the XRD probing deeper layers. The corresponding Ce 3d spectra of the fresh samples were typical of CeO₂. The spectrum in Fig. 12 obtained from the fresh Ni–Ce(WI) sample and representative also of the co-precipitated sample, was rather complex. The experimental curves were fitted with several components arising from the multiplicity of final states reached during the Ce 3d photoionization process [36]. The spectra contained also peaks such as *v'* and *u'* attributable to Ce³⁺ always present in pure CeO₂ and additionally generated under X-ray exposure. The Ce 3d was characterized by the main component (*v*) of the Ce 3d_{5/2} at 881.2 eV typical of Ce⁴⁺. The atomic ratios Ni/Ce of the two differently prepared samples were higher as compared to the nominal value of 0.2, with a much higher value for the sample prepared by impregnation. After the stability test at 800 °C this atomic ratio decreased in both samples, to a large extent in the impregnated one, indicative of sintering or inward diffusion of nickel. Quite peculiarly, the shape of the Ce 3d spectrum of the aged Ni–Ce(WI) changed drastically. Besides a slight increase of the Ce³⁺/Ce⁴⁺ ratio due to

the reducing conditions of the reaction, the spectrum contained additional peaks ~4 eV down energy shifted from the main peaks. Such features could be attributed to the differential charging effect originating from a not uniform distribution of conductive nickel particles among the semiconductor oxides [37]. This was particularly evident in the *u'''* component exhibiting a clear doublet. It is worth to notice that these additional peaks were not observed in the case of the co-precipitated sample. Such not quantifiable effect on the shape of the Ce 3d spectra could be a further confirmation of the stronger reduction undergone by the WI sample during the catalytic test, as evidenced by TPR and XRD results, and attributed to the larger CeO₂ crystallite sizes. The O 1s peak in these samples contained two components, a more intense one at 529.5 eV typical of CeO₂ and NiO and a weak one at 531.3 eV typical of hydroxide species such as Ce(OH)₃ or Ni(OH)₂ [38]. The XPS analyses of the Ni–La samples were discussed in terms of La 3d, O 1s and Ni 3p photoelectron peaks. Due to the overlap of Ni 2p_{3/2} with La 3d_{3/2} component [21] the information on nickel was obtained from the Ni 3p photoelectron transition at ~68 eV characteristic of Ni²⁺. The binding energy of La 3d_{5/2} at 834.5 eV was typical of La₂O₃. Also in this case two oxygen components were obtained, the more intense one at 531.5 eV due to La(OH)₃ or Ni(OH)₂ and the other weaker component at 529.0 eV due to La₂O₃ [39]. It was worth noticing that in these systems the Ni/La atomic ratios were practically the same, regardless the preparation method. Moreover after the stability test a slight increase of the ratio occurred, in clear contradiction with the Ni–Ce catalysts and in favor of a superior structural stability. With respect to the Ni–CeLa samples, as seen in Table 2, higher amounts of nickel and cerium were found on the surface of the impregnated samples as compared to the co-precipitated one. The differences was attributed to the different metal loading procedures which in the impregnated case favored the surface distribution of the nickel and, because of the double calcinations treatment of the CeLaO_x support, caused also the surface segregation of cerium. The Ni/(Ce + La) ratio decreased after the catalytic reaction, in agreement with the increased Ni crystallite sizes as given in Table 1.

To summarize, according to the XPS analyses, the La₂O₃ oxide imparted structural stability to the final Ni catalysts. Indeed, this oxide allowed, regardless the preparation procedure, a more uniform distribution of nickel which did not change after the stability test. The homogeneous distribution of nickel was likely due to the rapid formation of La_xNiO_y phases driving La³⁺ ions to the surface even in the case of the WI sample, producing a Ni/La surface atomic ratio slightly smaller than the nominal value of 0.2. As indicated by the XRD and Rietveld refinement analyses, the preparation procedure affected the composition of the mixed La_xNiO_y phases, the average Ni oxidation state and also the size of the support crystallites which were smaller in the case of the WI sample as compared to the CP one. From the structural and surface analyses

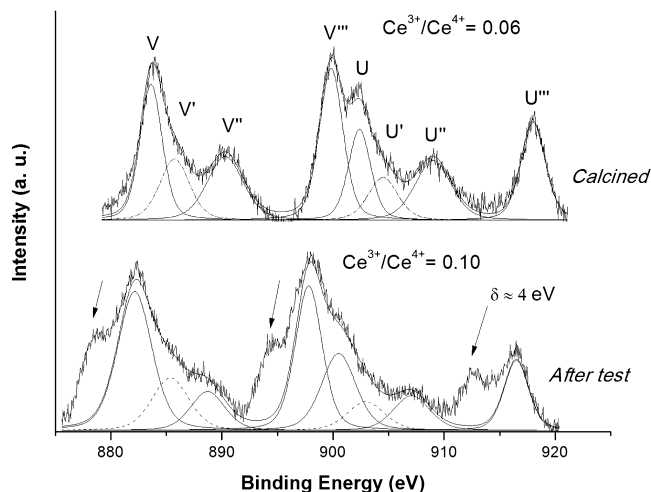


Fig. 12. Ce 3d XP spectra of Ni–Ce(WI) before and after the catalytic reaction.

the lower CPO light off temperature of the WI catalyst could be due to the small support crystallite size, favoring the nickel stabilization, whereas the higher and stable methane conversion at 800 °C could be due to a re-dispersion of the oxide phase, to a large extent in the CP sample, with no effect of the deposited carbon. Completely different situation occurred in the Ni–Ce samples. In this case the lack of a strong chemical interaction between nickel and cerium determined a procedure dependent surface Ni distribution with a remarkably larger Ni/Ce atomic ratio in the impregnated sample. However the co-precipitation of Ni and Ce ions produced smaller NiO and CeO₂ crystallite which favored a lower CPO reaction temperature but in a long run at 800 °C brought to a quick deactivation. The deactivation according to TGA was not caused by deposited carbon which in fact was found only on the stable Ni–Ce(WI) but, based on the XRD patterns of the aged samples, to less reducible and easier to sinter nickel species. Nickel over the mixed La₂O₃–CeO₂ oxide behaved similarly to the Ni–La systems, with the WI sample more active at lower temperature with respect to the CP sample and quite stable in the long run at 800 °C. Differently from the Ni–La system these catalysts did not form carbon under the experimental condition of the present study. The formation of a stable Ce_xLa_{1–x}O_a phase, in which the replacement of the Ce⁴⁺ with the trivalent La³⁺ ions enhanced the oxygen mobility, may have favored the transfer of the oxygen to the supported nickel, removing the carbon and avoiding coke formation [38].

4. Conclusion

The structural investigation on the Ni catalysts supported over CeO₂, La₂O₃ and mixed La₂O₃–CeO₂ indicated different interaction between the nickel and the support oxides modulated by the preparation procedure. In the case of the La₂O₃ oxide, the strong chemical interaction between nickel and lanthanum yielded a variety of mixed oxides going from LaNiO₃ to La₃Ni₁₂O₇. The interaction occurred with both, wet impregnation and co-precipitation, procedures. On the contrary, the CeO₂ support did not interact chemically with the oxidized Ni. However a reciprocal influence, enhanced by the co-precipitation method, produced smaller NiO and CeO₂ crystallites. In the case of the Ni over the mixed oxide, regardless the preparation procedure, stable Ce_xLa_{1–x}O_a phases were formed along with different amount of crystalline NiO and LaNiO₃. All the surveyed catalysts were very active in the CPO reaction. The smaller sizes of the precursor NiO and support crystallite oxides generally enhanced the activity at lower temperature. In a long run the strong deactivation observed for the Ni–Ce(CP), in the absence of carbon formation, was related to the lower reducibility and to the sintering of nickel. In none of the samples carbon deposition seemed to affect the catalyst stability. Nevertheless it was interesting to note that in the presence of the mixed CeO₂–La₂O₃ carbon did not form regardless the catalyst preparation procedure.

Acknowledgments

The Bilateral Collaboration Program supported by Italian CNR and Indian CSIR is kindly acknowledged.

The authors are thankful to Dr. Francesco Giordano from ISMN for performing the XRD measurements.

References

- [1] H. Wu, V. La Parola, G. Pantaleo, F. Puleo, A.M. Venezia, L.F. Liotta, *Catalysts* 3 (2013) 563–583.
- [2] M.-S. Fan, A.Z. Abdullah, S. Bhatia, *ChemSusChem* 4 (2011) 1643–1653.
- [3] A. Heinzl, B. Vogel, P. Hubner, *J. Power Source* 105 (2002) 202–207.
- [4] T.E. Rufford, S. Smart, G.C.Y. Watson, B.F. Graham, J. Boxall, J.C. Diniz da Costa, E.F. May, *J. Pet. Sci. Eng.* 94–95 (2012) 123–154.
- [5] S.A. Al-Sayari, *Open Catal. J.* 6 (2013) 17–28.
- [6] V.R. Choudhary, A.S. Mamman, *J. Chem. Technol. Biotechnol.* 73 (1998) 345–350.
- [7] B.C. Enger, R. Lødeng, A. Holmen, *Appl. Catal. A* 346 (2008) 1–27.
- [8] D.R. Lide (Ed.), *CRC Handbook of Chemistry and Physics*, CRC Press, New York, 2003.
- [9] L.D. Vella, J.A. Villoria, S. Specchia, N. Mota, J.L.G. Fierro, V. Specchia, *Catal. Today* 171 (2011) 84.
- [10] A.F. Lucredio, G. Jerkiewicz, E.M. Assaf, *Appl. Catal. B* 84 (2009) 106–111.
- [11] C. Song, W. Pan, *Catal. Today* 98 (2004) 463–484.
- [12] T. Zhu, M. Flytzani-Stephanopoulos, *Appl. Catal. A* 208 (2001) 403–417.
- [13] R.K. Singha, A. Shuka, S. Adak, C. Pendem, S. Saran, R. Bal, *Indian J. Chem.* 53A (2014), 467–171.
- [14] E. Ruckenstein, Y.H. Hu, *J. Catal.* 161 (1996) 55–61.
- [15] M. Fleys, Y. Simon, D. Swierczynski, A. Kiennemann, P.-M. Marquaire, *Energy Fuels* 16 (2006) 2321–2329.
- [16] M.D. Salazar-Villalpando, B. Reyes, *Int. J. Hydrogen Energy* 34 (2009) 9723–9729.
- [17] R. Pereñíguez, V.M. González-DelaCruz, J.P. Holgado, A. Caballero, *Appl. Catal. B* 93 (2010) 346–353.
- [18] S. Bhavar, G. Vesper, *Energy Fuels* 27 (2013) 2073–2084.
- [19] A.M. Venezia, L.F. Liotta, G. Pantaleo, A. Longo, in: A. Trovarelli, P. Fornasiero (Eds.), *Catalysis by Ceria and Related Materials*, Catalytic Science Series, vol. 12, 2nd ed., 2013.
- [20] V.A. Tsiporiari, Z. Zhang, X.E. Verykios, *J. Catal.* 179 (1998) 283–291.
- [21] J. Barbero, M.A. Pena, J.M. Campos-Martin, J.L.G. Fierro, P.L. Arias, *Catal. Lett.* 87 (2003) 211–217.
- [22] S.J. Gregg, K.S. Sing, *Adsorption, Surface Area and Porosity*, 2nd ed., Academic Press, San Diego, 1982.
- [23] JCPDS Powder Diffraction File, Int., Centre for Diffraction Data, Swarthmore, 1989.
- [24] A.C. Larson, R.B. von Dreele, GSAS, the General Structure Analysis System, Los Alamos National Laboratory, Los Alamos, 1991.
- [25] H.P. Klug, L.E. Alexander, *X-ray Diffraction Procedures for Polycrystalline and Amorphous Materials*, Wiley, New York, 1954.
- [26] D.A. Shirley, *Phys. Rev. B* 5 (1972) 4709–4714.
- [27] P.M.A. Sherwood, in: D. Briggs, M.P. Seah (Eds.), *Practical Surface Analysis*, Wiley, New York, 1990, p. 181.
- [28] S.C. Tsang, J.B. Claridge, M.L.H. Green, *Catal. Today* 23 (1995) 3–15.
- [29] S. Liang, E. Broitman, Y. Wang, A. Cao, G. Vesper, *J. Mater. Sci.* 46 (2011) 2928–2937.
- [30] F. Deganello, A. Martorana, *J. Solid State Chem.* 163 (2002) 527–533.
- [31] W. Shan, M. Luo, P. Ying, W. Shen, C. Li, *Appl. Catal. A* 246 (2003) 1–9.
- [32] A.M. Diskin, R.H. Cunningham, R.M. Ormerod, *Catal. Today* 46 (1998) 147–154.
- [33] J. Requies, M.A. Cabrero, V.L. Barrio, M.B. Guemez, J.F. Cambra, P.L. Arias, F.J. Perez-Alonso, M. Ojeda, M.A. Pena, J.L.G. Fierro, *Appl. Catal. A* 289 (2005) 214–223.
- [34] D. Guo, X. Zhang, J. Zhang, Y. Wang, *J. Mol. Catal. A* 269 (2007) 254–259.
- [35] P. Prieto, V. Nistor, K. Nouneh, M. Oyama, M. Abd-Leftil, R. Diaz, *Appl. Surf. Sci.* 258 (2012) 8807–8813.
- [36] A. Pfau, K.D. Schierbaum, *Surf. Sci.* 321 (1994) 71–80.
- [37] P. Fleming, S. Ramirez, J.D. Holmes, M.A. Morris, *Chem. Phys. Lett.* 509 (2011) 51–57.
- [38] L. Pino, A. Vita, M. Laganà, V. Recupero, *Appl. Catal. B* 148–149 (2014) 91–105.
- [39] M.F. Sunding, K. Hadidi, S. Diplas, O.M. Løvvik, T.E. Norby, A.E. Gunnæ, *J. Electron Spectrosc. Relat. Phenom.* 184 (2011) 399–409.